LITHOS 404–405 (2021) 106445

Contents lists available at ScienceDirect

LITHOS

journal homepage: www.elsevier.com/locate/lithos

Research Article

Tracing magma water evolution by H_2O-in-zircon: A case study in the Gangdese batholith in Tibet

Xiao-Ping Xia [a,b,c,*], Juntong Meng [a,d], Lin Ma [a,b], Christopher J. Spencer [e], Zexian Cui [a,b], Wan-Feng Zhang [a,b], Qing Yang [a,b], Le Zhang [a,b]

[a] State Key Laboratory of Isotope Geochemistry, Guangzhou Institute of Geochemistry, Chinese Academy of Sciences, Guangzhou 510640, China
[b] CAS Center for Excellence in Deep Earth Science, Guangzhou 510640, China
[c] Southern Marine Science and Engineering Guangdong Laboratory (Guangzhou), Guangzhou 511458, China
[d] College of Earth and Planetary Science, University of Chinese Academy of Sciences, Beijing 100049, China
[e] Department of Geological Sciences and Geological Engineering, Queen's University, Kingston, Ontario, Canada

ARTICLE INFO

Keywords:
H_2O-in-zircon
Zircon trace elements
Magma water content
Magmatic fluid evolution
Gangdese batholith

ABSTRACT

The presence of water has significant influence on magma properties such as the chemistry, viscosity, and crystallization temperature. Water content in the magma can be modified by magma replenishment or crystal fractionation, but technique for direct tracing of these processes are lacking. In this study, we analyzed zircon water content, oxygen isotopes, and trace element contents for a co-genetic granitic suite (one primitive biotite granite and two evolved garnet-bearing two-mica granites) from the Gangdese batholith in Tibet. The biotite granite shows a relatively narrow H_2O-in-zircon range with a sharp peak in the density plot, while multiple peaks are present for the garnet-bearing two-mica granites. The wide Hf range indicates that the zircon grains have a protracted magmatic history, and the positive H_2O vs. Hf correlation indicates that H_2O-in-zircon faithfully recorded the water variation of the evolving magma. These results suggest that H_2O-in-zircon is a good indicator to trace magma fluid evolution.

1. Introduction

Water plays a key role in many magmatic processes, including magma generation, crystallization, and volcanic eruption. Incorporation of water into nominally anhydrous minerals (NAMs) has been confirmed in the last decades (Bell and Rossman, 1992; Demouchy and Bolfan-Casanova, 2016; Peslier, 2010). Minor amounts of water in NAMs, expressed as hydrogen or hydroxyl, have significant impacts on rock physicochemical properties (Karato, 1990; Seaman et al., 2013). Water content in NAMs (e.g., olivine, pyroxene, and feldspar) has been widely used to calculate their magma or magma source H_2O content according to partition coefficients between magma and NAMs (Okumura, 2011; Xia et al., 2013). Zircon is a common NAM in intermediate-felsic rocks, and is widely used for U—Pb dating (Pidgeon et al., 2017; Wu and Zheng, 2004) and Hf-O-Li isotope tracing of magma source character (Trail et al., 2007; Trail et al., 2018; Ushikubo et al., 2008; Valley, 2003; Xia et al., 2006). However, little attention was given to water content in zircon due to analytical challenge and limitation on using H_2O-in-zircon to calculate the magma water content (De Hoog et al., 2014; Xia et al., 2019). The limited data available led to contradictory claims that crystalline zircon can accommodate only low H_2O (<100 μg/g) (Bell, 2004; Woodhead et al., 1991b) or more than 1000 μg/g H_2O (De Hoog et al., 2014). Therefore, it remains unclear whether H_2O-in-zircon can be used as a magma water content indicator or not. There is a general concept of increasing water in the evolving magma due to crystallization fractionation. In order to test H_2O-in-zircon can record this evolution or not, in this contribution we analyzed the water content and oxygen isotope compositions of zircon grains from a co-magmatic granite suite in the Gangdese batholith, including a less-evolved biotite granite (also called normal granite) and two more-evolved granites, which emplaced coevally at ~62 Ma in Zhengga area, southern Tibet (Ma et al., 2017).

2. Sample descriptions

The samples used in this study were described in detail by Ma et al. (2017). They were collected from the Zhengga area of southern Tibet

* Corresponding author at: State Key Laboratory of Isotope Geochemistry, Guangzhou Institute of Geochemistry, Chinese Academy of Sciences, Guangzhou 510640, China.
E-mail address: xpxia@gig.ac.cn (X.-P. Xia).

https://doi.org/10.1016/j.lithos.2021.106445
Received 29 October 2020; Received in revised form 30 August 2021; Accepted 31 August 2021
Available online 3 September 2021

(Fig. 1). Ma et al. (2017) has also given a detailed account on the field geological and petrographic characteristics, geochemistry of whole rock and rock-forming minerals, and tectonic setting of the samples. The granite suite consists mainly of biotite granite (BG) and garnet-bearing two-mica granite (GBG), and was emplaced in the Paleocene (ca. 62 Ma) during the incipient India-Asia collision (Hu et al., 2017; Mo et al., 2008). The close field association, and the nearly identical ages, whole-rock Sr—Nd and zircon Hf—O isotope compositions between BG and GBG indicate that they were derived from a same juvenile crustal-dominated source (Ma et al., 2017). However, the BGs are characterized by higher MgO (0.4–0.7 wt%) but lower SiO_2 (70–73 wt%) and A/CNK (0.98–1.08) than the GBGs (SiO_2 = 73–76 wt%, MgO <0.3 wt%, A/CNK = 1.03–1.21). Geochemical modeling indicates that fractionation of K-feldspar, biotite and titanite and minor plagioclase and accessory minerals (zircon, apatite, allanite and monazite) can account for their compositional variation (Ma et al., 2017). The mineral compositional difference also supports that the GBGs represent a more-fractionated product. The biotite in the GBG has lower TiO_2 and MgO contents than that in the BG. In addition, the plagioclase composition evolves from andesine through oligoclase to albite for BG and GBG. Garnet grains in the GBG become increasingly almandine from core to rim. Garnet and mica in the GBG were likely formed by reaction between biotite and (Mn, Al)-rich magma.

One BG (11SR04) and two GBG (11SR05–2 and 09 TB66) samples were selected for the zircon water content and oxygen isotope analyses. Sample 11SR04 has SiO_2 = 71.87 wt%, A/CNK = 1.04, Zr/Hf = 29.3, Eu/Eu* = 0.64, whereas samples 11SR05–2 and 09 TB66 have SiO_2 = 73.99 and 75.01 wt%, A/CNK = 1.09 and 1.21, Zr/Hf = 20.1 and 22.8, Eu/Eu* = 0.14 and 0.10, respectively (Ma et al., 2017).

3. Analytical methods

Zircon grains were separated from crushed rock samples by conventional heavy liquid and magnetic methods. The separated zircon grains were placed on a double-sided adhesive tape, and then molten tin-based alloy was poured into hollow cylinder above the adhesive tape for mounting. Detailed sample preparation procedures were described by Zhang et al. (2018). Cathodo-luminescence (CL) imaging of zircon grains was obtained in order to observe the inner structure and choose potential target sites for analyses at the State Key Laboratory of Isotope Geochemistry, Guangzhou Institution of Geochemistry, Chinese Academy of Sciences (GIGCAS), using a CAMECA SE-50 microprobe.

3.1. Water content and oxygen isotope analyses

Water content in NAMs is most commonly measured with the Fourier transform infrared spectroscopy (FTIR) due to its high sensitivity and ability to distinguish hydrogen species and association with cations (Trail et al., 2011; Woodhead et al., 1991b). However, FTIR method was unsuitable for our zircon samples due to their small grain size (about 100 μm). In this study, zircon water content and oxygen isotope were measured simultaneously by a large geometry secondary ion mass spectrometry (LG-SIMS) CAMECA IMS 1280-HR at GIGCAS. To improve the vacuum performance, liquid nitrogen was used to cool the sample chamber via an automatic liquid nitrogen refilling system developed by Zhang et al. (2018). Before the analysis, the alloy mount was kept in the storage chamber overnight.

A 3–5 nA Cs^+ primary beam was accelerated at 10 kV and the secondary ion beam was extracted with −10 kV energy. A normal incidence electron gun was used to compensate the charge near the analytical spot. ^{16}O and ^{18}O were collected by two Faraday cup detectors with resistors of 10^{10} and 10^{11} Ohm, respectively, while $^{16}O^1H$ was detected by an

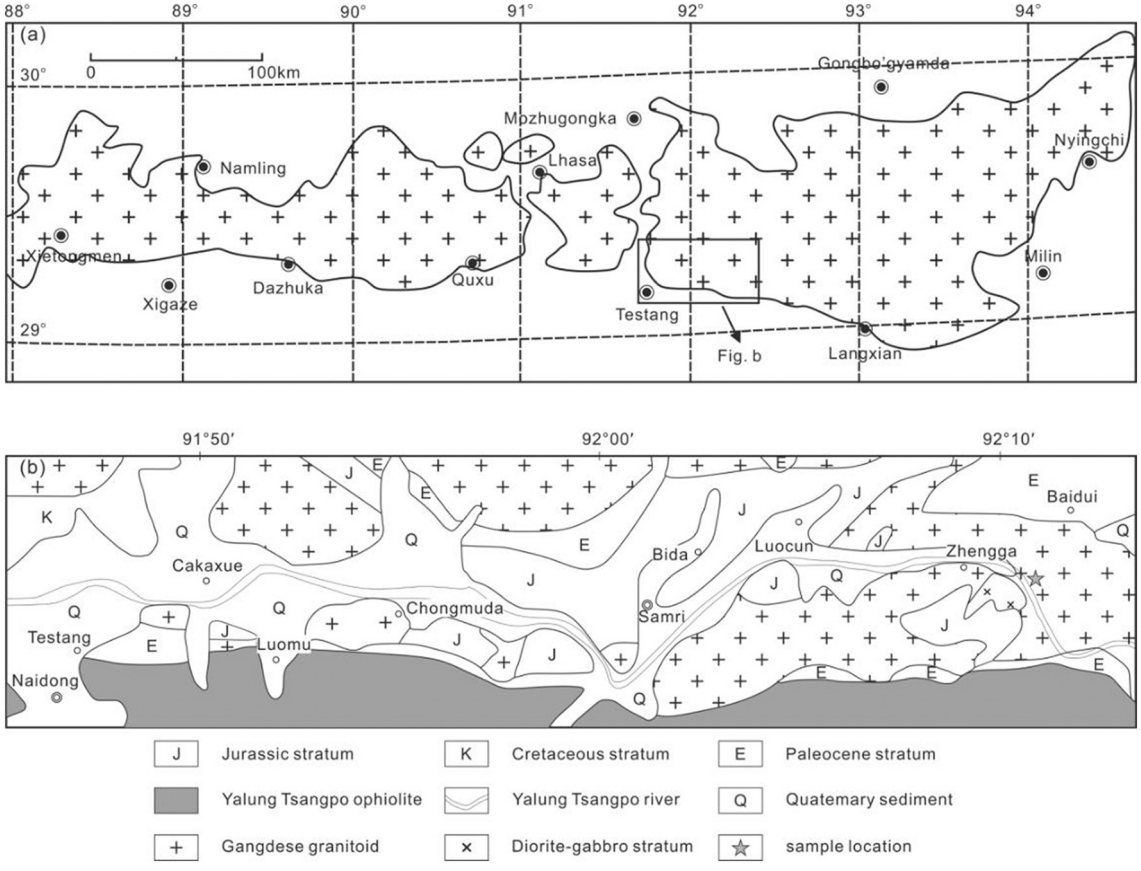

Fig. 1. Geological maps of (a) Gangdese batholith in Xigaze-Nyingchi area and (b) Samri area, showing the sampling locations.

electron multiplier. Collector slits of 500 μm was used to collect ^{16}O and ^{18}O, corresponding to a mass resolving power of ca. 2500. To minimize the ^{17}O interference, a ~ 173 nm collector slit was used for $^{16}O^{1}H$, which yielded a mass resolving power of ca. 7000. The magnetic field was locked using nuclear magnetic resonance (NMR) probe by regulation mode. Single analytical run contains ca. 200 s of pre-sputtering and beam alignment (centering DTFA and DTCA). A total of 60 s were used for data acquisition with 16 integrated cycles. Measured $^{16}O^{1}H/^{16}O$ ratios were calibrated into H_2O contents based on the calibration curve established by FTIR results and SIMS $^{16}O^{1}H/^{16}O$ ratios for a set of zircon reference matrials (Xia et al., 2019). The oxygen isotope compositions were normalized to the Vienna Standard Mean Ocean Water compositions (SMOW) notated as $\delta^{18}O_M$, and calibrated with zircon SA01 standard with the recommended $\delta^{18}O = 6.16 \pm 0.26‰$ (Huang et al., 2020).

3.2. Trace element analysis

Zircon trace element concentrations were measured at GIGCAS, using an inductively coupled plasma-sector field-mass spectrometer (ICP-SF-MS) instrument of ELEMENT XR equipped with a Resonetic RESOlution M-50193 nm ArF excimer laser ablation system. Laser ablation was conducted at a 5 Hz repetition rate, ~4 J/cm^2 energy density, and 33 μm spot size. Analysis time of a single spot was 50s, consisting of 20s laser-off background acquisition and 30s laser-on sample data acquisition. Helium was used as a carrier gas for aerosol transport. The following masses were measured: ^{25}Mg, ^{27}Al, ^{29}Si, ^{31}P, ^{49}Ti, ^{57}Fe, ^{89}Y, ^{139}La, ^{140}Ce, ^{141}Pr, ^{145}Nd, ^{149}Sm, ^{151}Eu, ^{155}Gd, ^{159}Tb, ^{163}Dy, ^{165}Ho, ^{167}Er, ^{169}Tm, ^{172}Yb, ^{175}Lu, ^{178}Hf. The reference materials of NIST SRM 610 and NIST SRM 612 are bracketed into the unknown sample sequence. NIST SRM 610 was used as the external standard for mass bias calibration and instrumental drift, whilst ^{29}Si was used as the internal standard. Detailed analytical procedures and the data reduction strategy were described by Zhang et al. (2019). NIST 612 was used as unknown to check the analytical reliability. The average results for NIST 612 analysis yielded good consistency with the recommended value, and the analytical error and precision are within 10%.

4. Results

4.1. Zircon CL imaging

Representative zircon cathodoluminescence (CL) images were shown in Fig. 2. Nearly all zircon grains are euhedral-subhedral prismatic. Zircon grains from the BG sample 11SR04 are generally larger (50–250 μm) than zircons from the GBG samples (50–150 μm). The grains analyzed show magmatic zircon characteristics, including oscillatory zoning and core-rim texture.

4.2. Zircon water content and oxygen isotopes

All the H_2O content and oxygen isotope data obtained are listed in Supplementary Table 1. Six spots were excluded due to their large $^{16}O^{1}H/^{16}O$ uncertainties and/or extremely high Al and Y contents, which likely reflect contamination by nano-sized H_2O-rich inclusions, or zone lamellae (Pidgeon et al., 2019; Xia et al., 2019). Previous studies showed that as non-formula elements, Al and Y can penetrate fractures and selected zone lamellae during weathering (Pidgeon et al., 2019). As shown in Fig. 3, the less-evolved BG sample 11SR04 has water-in-zircon

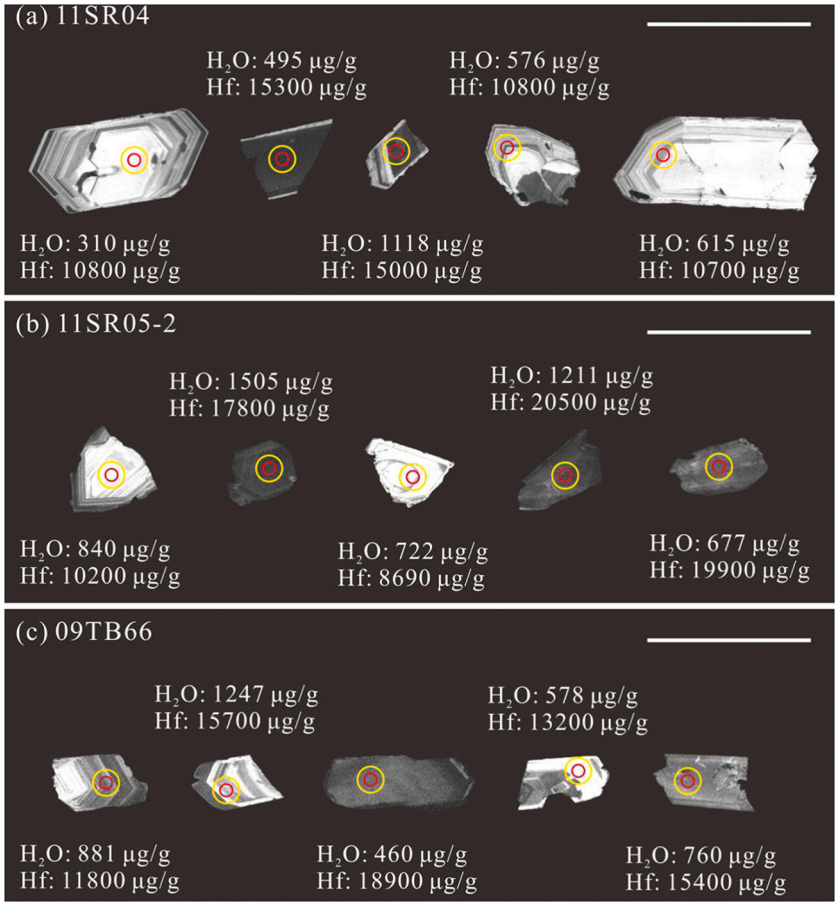

Fig. 2. Representative zircon CL images. Red and yellow circles denote the SIMS and LA-ICPMS analysis spots, respectively. (For interpretation of the references to colour in this figure legend, the reader is referred to the web version of this article.)

of 203–2339 μg/g (median 566 μg/g). It shows one main sharp peak at 515 μg/g in the kernel density plot (Fig. 4a). The two evolved GBG samples 11SR05–2 and 09 TB66 have water-in-zircon of 279–2216 μg/g and 112–2193 μg/g, respectively. Compared with the BG, the GBGs have higher median water-in-zircon values (11SR05–2: 883 μg/g; 09 TB66: 734 μg/g) (Fig. 3). Also, the two GBG samples have wider interquartile range than the BG (Fig. 3), indicating greater dispersion (>1000 μg/g). The kernel density plot shows a bimodal distribution peak at 410 and 1070 μg/g, and 590 and 1230 μg/g, respectively (Fig. 4b, c).

All three samples have similar zircon $\delta^{18}O$ compositions (Fig. 5). The BG sample have zircon $\delta^{18}O$ = +5.71 – +7.82‰. The GBG samples 11SR05–2 and 09 TB66 have zircon $\delta^{18}O$ = 5.18–7.21‰ and 4.69–6.38‰, respectively. The measured $\delta^{18}O$ values have no obvious correlation with the H_2O contents (Fig. 5).

4.3. Trace element compositions

The results are listed in Supplementary Table 2. Compared with the BG sample, the two GBG samples have higher zircon Hf and REE concentrations. Zircon grains separated from the BG have a smaller Hf range (ca. 7000–16,000 μg/g) than grains from the GBG (Hf = ca. 7000–24,700 μg/g). One spot was discarded due to its very high Ti content (59.8 μg/g), possibly caused by contamination. The Ti contents of BG and GBG cluster in the 0.69–11.1 μg/g range. Zircon grains from all the three samples show negative Eu anomalies (Eu/Eu* ($Eu_N/(Sm_N \times Gd_N)^{0.5}$) = 0–0.8), while the BG zircons have higher Eu/Eu* values of (0.1–0.8) than the GBG ones (Eu/Eu* <0.1) (Fig. 6).

5. Discussion

5.1. Radiation damage in the zircon samples

Radiation damage accumulated by radioactive U—Th decay can cause zircon metamictization (Chakoumakos et al., 1987; Murakami et al., 1991; Nasdala et al., 2002). Metamict zircon exhibits distinctive density, unit-cell parameter, refractive index, and fracturing (Chakoumakos et al., 1987). Previous works indicated that metamict zircons with high degree of damage may contain abundant secondary water (up to 16 wt%) (Nasdala et al., 2001; Pidgeon et al., 2017; Wang et al., 2018; Woodhead et al., 1991a; Woodhead et al., 1991b), which may be related to the post-hydrothermal alteration where exotic cations enter the low-atomic-density metamict zircon (Geisler et al., 2002).

To check whether our zircon samples are metamictized or not, we calculated the radiation dose Dα based on the U—Th abundance and U—Pb age data reported by Ma et al. (2017). The cumulated Dα for all zircon grains is far below the damage threshold (< 3 × 10^{15} α decay event/mg) proposed by Murakami et al. (1991) (Supplementary

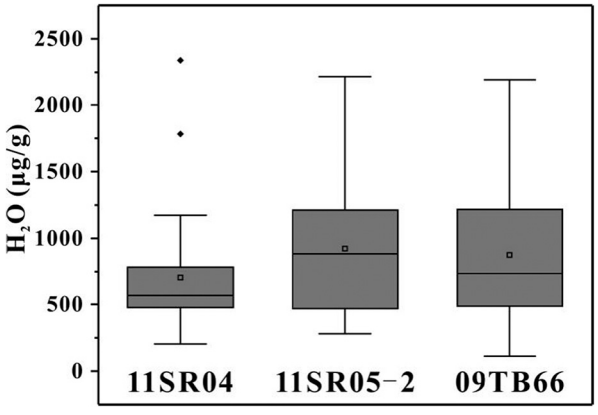

Fig. 3. Box plots of zircon H_2O contents for the Gangdese batholith. Rectangles represent the average value of each sample.

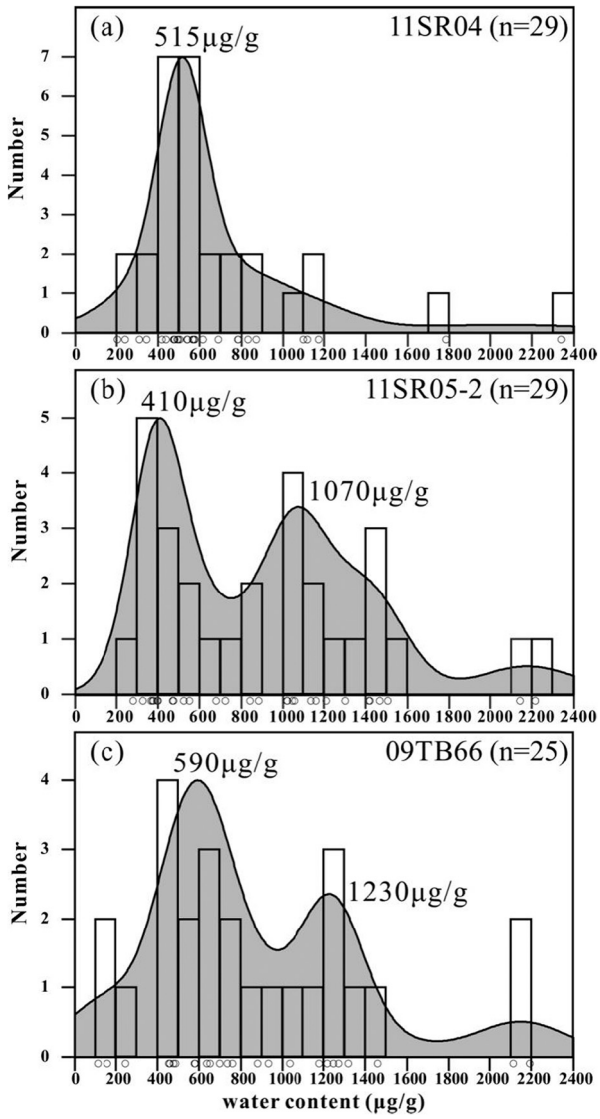

Fig. 4. Kernel density estimation plots, showing the water-in-zircon distributions. Peak values are annotated.

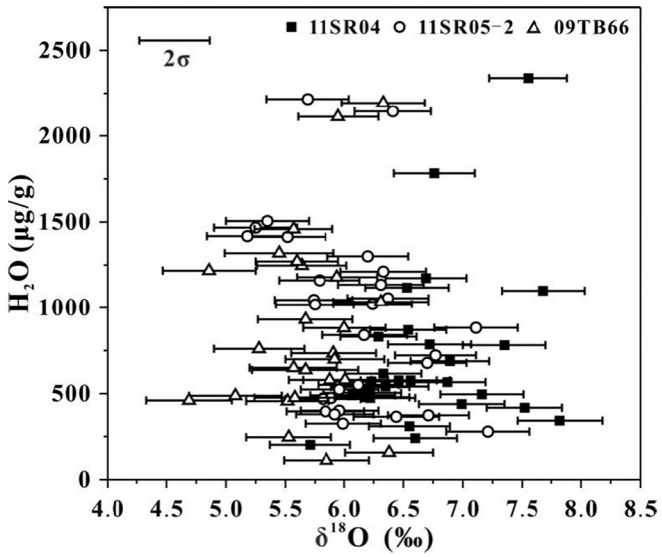

Fig. 5. Plot of H_2O content vs. $\delta^{18}O$, indicating no correlation between them.

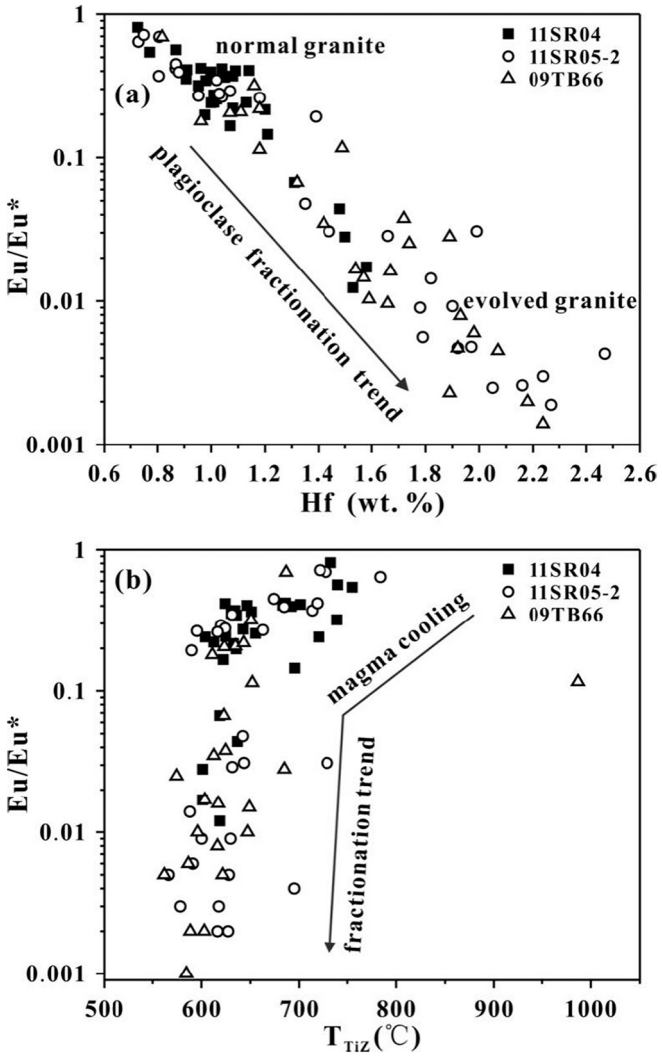

Fig. 6. Plots of zircon Eu/Eu*versus (a) Hf content and (b) T_{Tiz} (°C).

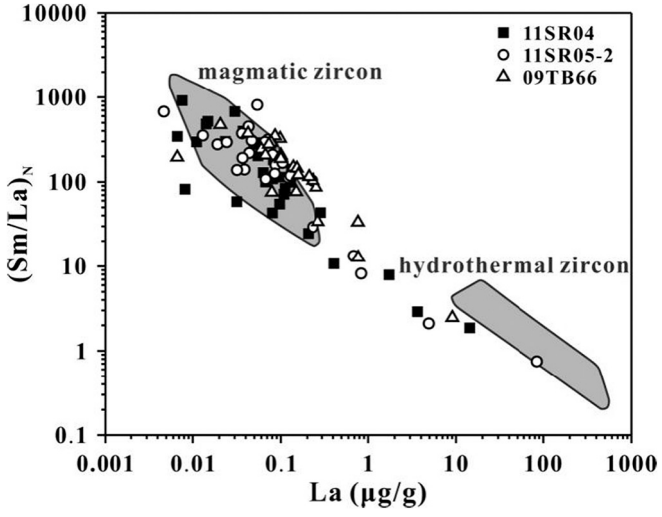

Fig. 7. Chondrite-normalized Sm/La vs. La plot. The magmatic and hydrothermal zircon fields were from Hoskin (2005). Chondrite normalizing values are from Sun and McDonough (1989).

Table 3). Except for five spots with high La content (possibly due to impurity), most zircon analyses have high $(Sm/La)_N$ and low La content (Fig. 7), resembling typical magmatic crystalline zircons (Hoskin, 2005).

5.2. Charge balance between trace elements in zircon

Zircon is commonly enriched in tetravalent U, Th, and Hf due to their substitution of Zr^{4+}. Trivalent cations, including REE, Y and Al are also abundant in zircon (Finch, 2003; Hoskin and Schaltegger, 2003). To maintain charge balance, a coupled substitution (termed as xenotime substitution) was proposed, in which P^{5+} and $(REE + Y)^{3+}$ are coupled to replace Si^{4+} or Zr^{4+}. Accordingly, the (REE + Y)/P molar ratio should be equal to one. However, De Hoog et al. (2014) found that natural zircon samples from a oceanic gabbro have excess of (REE + Y) to P, and the (REE + Y) excess is well balanced by H as the (H + P)/(REE + Y) molar ratios are equal to/ approaching one. This suggests that the H_2O content is possibly controlled by charge-balance between H, P, and (REE + Y) in crystalline zircon, and that using zircon water content to constrain the magma water content is not straightforward (De Hoog et al., 2014). In the molar (REE + Y) vs. (H + P) plot, our data points fall mostly in the field of (H + P)/(REE + Y) > 1 (Fig. 8a), and three spots show P excess (i.e., above the 1:1 line) (Fig. 8b), which also yield obvious H. This indicates that charge balance for excess (REE + Y) to P is not the only way for H-uptake in our zircon samples.

5.3. Water evolution during magma fractionation and its records in zircon

As water is incompatible, its content would increase with magma fractionation (Petrelli et al., 2018). The whole-rock Zr/Hf ratios of the GBG samples (11SR05–2 = 20.1, 09 TB66 = 22.8) are lower than that of the BG sample (29.3), and outside the "CHARAC" (CHArge and RAdius Controlled) range (26–46), suggesting that the GBG magma was "wet" (Bau, 1996). In addition, the negative Eu anomaly, the low ∑ REE contents and LREE/HREE ratios for the GBG are also consistent with a volatile-rich magma system (Wu et al., 2017). This indicates that the more-evolved GBG magma was more volatile-rich than the BG magma.

Besides, the less evolved granite and evolved granite can be distinguished according to the zircon Hf content and Zr/Hf ratio (Breiter et al., 2014). High Hf content (>1.2 wt%) and low Zr/Hf (<55) are characteristics of zircon crystallized in evolved magmas (Claiborne et al., 2006; Claiborne et al., 2010; Deering et al., 2016). The BG has their zircon Zr/Hf > 55, supporting its less-evolved nature (Breiter et al., 2014). In contrast, nearly 40% of the zircon grains from the GBG have Zr/Hf < 55, indicating their crystallization from a more evolved magma (Supplementary Table 2). In the Hf vs. Eu/Eu* plot (Fig. 6a), the BG zircon analyses mostly plot at one end of the normal granite field (Hf < 17,000 μg/g and Eu/Eu* > 0.05), whereas the GBG zircon grains show a wide composition range toward the evolved granite end-member (Fig. 6a). We interpreted these zircon grains to have crystallized during or after plagioclase fractional crystallization (Deering et al., 2016; Yan et al., 2018). Ti-in-zircon thermometer (Ferry and Watson, 2007) is another commonly used tool to obtain crystallization temperature. Assuming that $\alpha_{SiO2} = 1$ and $\alpha_{TiO2} = 0.75$, the calculated temperature correlate positively with Eu/Eu* when Eu/Eu* > 0.1. Most zircon grains from the BG plotted in this field (Fig. 6b), indicating that they were crystallized progressively with the magma cooling without significant plagioclase fractionation. In contrast, most GBG zircon samples show a steep downtrend of Eu/Eu* with nearly constant temperature (Fig. 6b). This suggests that the crystallization of most GBG zircon grains was associated with significant plagioclase fractionation, although some zircon grains may have crystallized in the early hotter magma similar to the BG zircon.

In Fig. 9a, the positive Hf vs. H_2O correlation indicates a H_2O-in-zircon rise with magma evolution and increasing magma water content. In the H_2O-in-zircon density plot (Fig. 4a), the BG zircon samples show a H_2O content peak at 515 μg/g, indicating that most zircon grains were

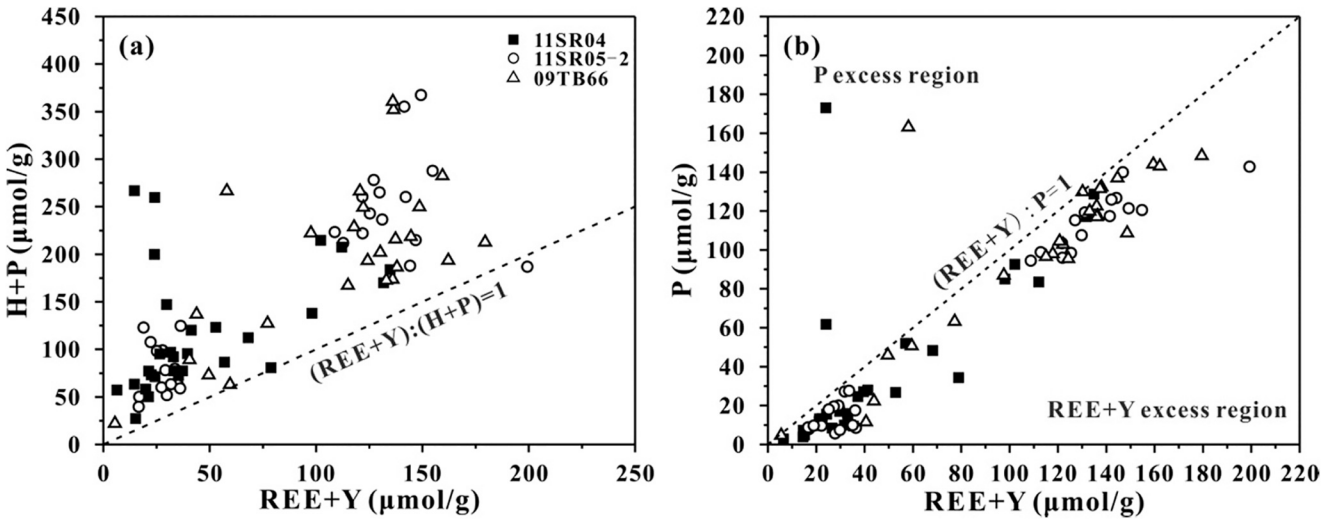

Fig. 8. Plots of zircon (a) (H + P) vs. (REE + Y) and (b) P vs. (REE + Y).

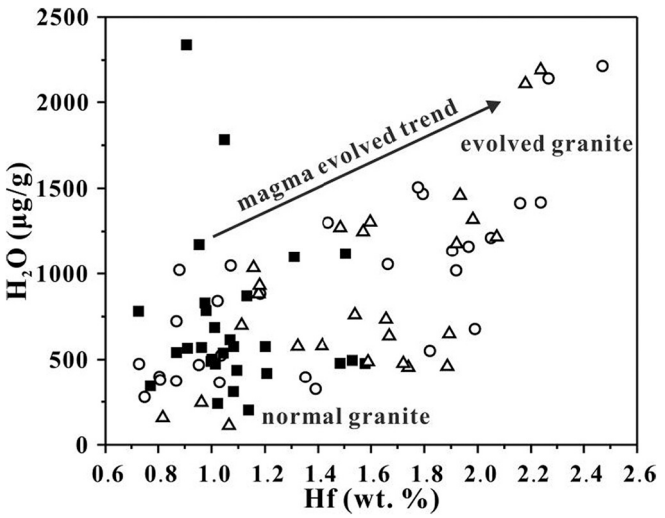

Fig. 9. Plot of zircon H_2O versus Hf content.

crystallized in a magma with similar water content. In contrast, both GBG samples yielded a wide-range and multiple populations (Fig. 2b-c). The recent study of Samperton et al. (2017) has shown that zircon from plutonic rocks may have a protracted crystallization history between the temperature of zircon saturation and rock solidification. We interpreted our GBG H_2O-in-zircon results to have recorded such protracted crystallization history. It is noteworthy that both samples have a major H_2O-in-zircon peak similar to that of the BG sample (400–600 μg/g, Fig. 4), which means that these zircon grains were crystallized at the initial stage, when the magma water content was comparable with the BG magma. This interpretation is consistent with their co-magmatic petrogenesis based on petrological and geochemical evidence (Ma et al., 2017). In addition, we have reported H_2O-in-zircon results of two less-evolved granitoids in the Gangdese belt, which show similar results with the BG such as one dominant peak in 400–600 μg/g (Meng et al., 2021), which means that these mamas have similar initial water content and the higher water content for evolved GBG magma is the result of magma evolution. Consequently, we considered that the water content of zircon in the Zhengga granites records the water content increase from BG to GBG.

6. Conclusions

Secondary ion mass spectrometry (SIMS) results show distinct water contents in crystalline zircon from the Gangdese granites with different degrees of evolution. The median water-in-zircon of the less-evolved biotite granite and the co-magmatic more-evolved garnet-bearing two-mica granite were around 566 and 750–900 μg/g, respectively. The biotite granite sample shows a single dominant H_2O-in-zircon peak in the kernel density plot, while the garnet-bearing two-mica granites have multiple H_2O-in-zircon peaks, indicating a protracted crystallization history of this granitic suite. Zircon grains with high water content (>1000 μg/g) are also characterized by higher Hf content and lower Eu/Eu*, indicating that these grains were crystallized in highly-evolved magma with high volatile content. This demonstrates that H_2O-in-zircon is a good indicator of magma water content. We suggested that the water incorporation into zircon is not entirely controlled by charge balance, and that the magmatic water content is a major controlling factor on H_2O-in-zircon.

Declaration

No conflict of interest exits in the submission of this manuscript, and manuscript is approved by all authors for publication. I would like to declare on behalf of my co-authors that the work described was original research that has not been published previously, and is not under consideration for publication elsewhere, in whole or in part.

Declaration of Competing Interest

None.

Acknowledgements

We thank Yanqiang Zhang for helping with the zircon sample preparation. This research is financially supported by the National Key R&D Program of China (2018YFA0702600) and the National Science Foundation of China (41673010). This is a contribution of the Chemical Geodynamic Joint Laboratory between the CAS GIG (No. IS-3068) and the University of Hong Kong.

Appendix A. Supplementary data

Supplementary data to this article can be found online at https://doi.org/10.1016/j.lithos.2021.106445.

References

Bau, M., 1996. Controls on the fractionation of isovalent trace elements in magmatic and aqueous systems: evidence from Y/Ho, Zr/Hf, and lanthanide tetrad effect. Contrib. Mineral. Petrol. 123, 323–333.

Bell, D.R., 2004. Abundance and Partitioning of OH in a High-pressure Magmatic System: Megacrysts from the Monastery Kimberlite, South Africa. J. Petrol. 45, 1539–1564.

Bell, D.R., Rossman, G.R., 1992. Water in Earth's Mantle: the Role of Nominally Anhydrous Minerals. Science 255, 1391–1397.

Breiter, K., Lamarão, C.N., Borges, R.M.K., Dall'Agnol, R., 2014. Chemical characteristics of zircon from A-type granites and comparison to zircon of S-type granites. Lithos 192-195, 208–225.

Chakoumakos, B.C., MURAKAMI, T., LUMPKIN, G.R., EWING, R.C., 1987. Alpha-Decay–Induced Fracturing in Zircon: the transition from the Crystalline to the Metamict State. Science 236, 1556–1559.

Claiborne, L., Miller, C.F., Walker, B.A., Wooden, J.L., Mazdab, F.K., Bea, F., 2006. Tracking magmatic processes through Zr/Hf ratios in rocks and Hf and Ti zoning in zircons: An example from the Spirit Mountain batholith, Nevada. Mineral. Mag. 70, 517–543.

Claiborne, L.L., Miller, C.F., Wooden, J.L., 2010. Trace element composition of igneous zircon: a thermal and compositional record of the accumulation and evolution of a large silicic batholith, Spirit Mountain, Nevada. Contrib. Mineral. Petrol. 160, 511–531.

De Hoog, J.C.M., Lissenberg, C.J., Brooker, R.A., Hinton, R., Trail, D., Hellebrand, E., Eimf, 2014. Hydrogen incorporation and charge balance in natural zircon. Geochim. Cosmochim. Acta 141, 472–486.

Deering, C.D., Keller, B., Schoene, B., Bachmann, O., Beane, R., Ovtcharova, M., 2016. Zircon record of the plutonic-volcanic connection and protracted rhyolite melt evolution. Geology 44, 267–270.

Demouchy, S., Bolfan-Casanova, N., 2016. Distribution and transport of hydrogen in the lithospheric mantle: a review. Lithos 240-243, 402–425.

Ferry, J.M., Watson, E.B., 2007. New thermodynamic models and revised calibrations for the Ti-in-zircon and Zr-in-rutile thermometers. Contrib. Mineral. Petrol. 154, 429–437.

Finch, R.J., 2003. Structure and Chemistry of Zircon and Zircon-Group Minerals. Rev. Mineral. Geochem. 53, 1–25.

Geisler, T., Pidgeon, R.T., van Bronswijk, W., Kurtz, R., 2002. Transport of uranium, thorium, and lead in metamict zircon under low-temperature hydrothermal conditions. Chem. Geol. 191, 141–154.

Hoskin, P.W.O., 2005. Trace-element composition of hydrothermal zircon and the alteration of Hadean zircon from the Jack Hills, Australia. Geochim. Cosmochim. Acta 69, 637–648.

Hoskin, P.W.O., Schaltegger, U., 2003. The composition of zircon and igneous and metamorphic petrogenesis, pp. 27–62.

Hu, X., Wang, J., An, W., Garzanti, E., Li, J., 2017. Constraining the timing of the India-Asia continental collision by the sedimentary record. Sci. China Earth Sci. 60, 603–625.

Huang, C., Wang, H., Yang, J.-H., Ramezani, J., Yang, C., Zhang, S.-B., Yang, Y.-H., Xia, X.-P., Feng, L.-J., Lin, J., Wang, T.-T., Ma, Q., He, H.-Y., Xie, L.-W., Wu, S.-T., 2020. SA01 – a Proposed Zircon Reference Material for Microbeam U-Pb Age and Hf-O Isotopic Determination. Geostand. Geoanal. Res. 44, 103–123.

Karato, S., 1990. The role of hydrogen in the electrical conductivity of the upper mantle. Nature 347, 272–273.

Ma, L., Wang, Q., Kerr, A.C., Yang, J.-H., Xia, X.-P., Ou, Q., Yang, Z.-Y., Sun, P., 2017. Paleocene (c. 62 Ma) Leucogranites in Southern Lhasa, Tibet: Products of Syn-collisional Crustal Anatexis during Slab Roll-back? J. Petrol. 58, 2089–2114.

Meng, J., Xia, X., Ma, L., Jiang, Z., Xu, J., Cui, Z., Yang, Q., Zhang, W., Zhang, L., 2021. A H2O-in-zircon perspective on the heterogeneous water content of crust-derived magmas in southern Tibet. Sci. China Earth Sci. 64, 1184–1194.

Mo, X., Niu, Y., Dong, G., Zhao, Z., Hou, Z., Zhou, S., Ke, S., 2008. Contribution of syncollisional felsic magmatism to continental crust growth: a case study of the Paleogene Linzizong volcanic Succession in southern Tibet. Chem. Geol. 250, 49–67.

Murakami, T., Chakoumakos, B.C., Ewing, R.C., Lumpkin, G.R., Weber, W.J., 1991. Alpha-decay event damage in zircon. Am. Mineral. 76 (9–10), 1510–1532.

Nasdala, L., Beran, A., Libowitzky, E., Wolf, D., 2001. The incorporation of hydroxyl groups and molecular water in natural zircon (ZrSiO4). Am. J. Sci. 301, 831–857.

Nasdala, L., Lengauer, C.L., Hanchar, J.M., Kronz, A., Wirth, R., Blanc, P., Kennedy, A.K., Seydoux-Guillaume, A.-M., 2002. Annealing radiation damage and the recovery of cathodoluminescence. Chem. Geol. 191, 121–140.

Okumura, S., 2011. The H2 O content of andesitic magmas from three volcanoes in Japan, inferred from the infrared analysis of clinopyroxene. Eur. J. Mineral. 23, 771–778.

Peslier, A.H., 2010. A review of water contents of nominally anhydrous natural minerals in the mantles of Earth, Mars and the Moon. J. Volcanol. Geotherm. Res. 197, 239–258.

Petrelli, M., El Omari, K., Spina, L., Le Guer, Y., La Spina, G., Perugini, D., 2018. Timescales of water accumulation in magmas and implications for short warning times of explosive eruptions. Nat. Commun. 9, 770.

Pidgeon, R.T., Nemchin, A.A., Whitehouse, M.J., 2017. The effect of weathering on U–Th–Pb and oxygen isotope systems of ancient zircons from the Jack Hills, Western Australia. Geochim. Cosmochim. Acta 197, 142–166.

Pidgeon, R.T., Nemchin, A.A., Roberts, M.P., Whitehouse, M.J., Bellucci, J.J., 2019. The accumulation of non-formula elements in zircons during weathering: Ancient zircons from the Jack Hills, Western Australia. Chem. Geol. 530, 119310.

Samperton, K.M., Bell, E.A., Barboni, M., Keller, C.B., Schoene, B., 2017. Zircon age-temperature-compositional spectra in plutonic rocks. Geology 45 (11), 983–986.

Seaman, S.J., Williams, M.L., Jercinovic, M.J., Koteas, G.C., Brown, L.B., 2013. Water in nominally anhydrous minerals: Implications for partial melting and strain localization in the lower crust. Geology 41, 1051–1054.

Sun, S.S., McDonough, W.F., 1989. Chemical and Isotopic Systematics of Oceanic Basalts: Implications for Mantle Composition and Processes (Geological Society).

Trail, D., Mojzsis, S., Harrison, T., Schmitt, A., Watson, E., Young, E., 2007. Constraints on Hadean zircon protoliths from oxygen isotopes, Ti-thermometry, and rare earth elements. Geochem. Geophys. Geosyst. 8, 6014.

Trail, D., Thomas, J.B., Watson, E.B., 2011. The incorporation of hydroxyl into zircon. Am. Mineral. 96, 60–67.

Trail, D., Boehnke, P., Savage, P., Liu, M.-C., Miller, M., Bindeman, I., 2018. Origin and significance of Si and O isotope heterogeneities in Phanerozoic, Archean, and Hadean zircon. Proc. Natl. Acad. Sci. 115, 201808335.

Ushikubo, T., Kita, N.T., Cavosie, A.J., Wilde, S.A., Rudnick, R.L., Valley, J.W., 2008. Lithium in Jack Hills zircons: evidence for extensive weathering of Earth's earliest crust. Earth Planet. Sci. Lett. 272, 666–676.

Valley, J.W., 2003. Oxygen Isotopes in Zircon. Rev. Mineral. Geochem. 53, 343–385.

Wang, R., Jeon, H., Evans, N.J., 2018. Archaean hydrothermal fluid modified zircons at Sunrise Dam and Kanowna Belle gold deposits, Western Australia: Implications for post-magmatic fluid activity and ore genesis. Am. Mineral. 103, 1891–1905.

Woodhead, J.A., Rossman, G.R., Silver, T., 1991a. The Metamictization of Zircon: radiation Dose-Dependent Structural Characteristics. Am. Mineral. 76, 1–2.

Woodhead, J.A., Rossman, G.R., Thomas, A.P., 1991b. Hydrous species in zircon. Am. Mineral. 76, 1533–1546.

Wu, Y., Zheng, Y.-F., 2004. Genesis of zircon and its constraints on interpretation of U-Pb age. Chin. Sci. Bull. 49, 1554–1569.

Wu, F., Liu, X., Ji, W., Wang, J., Yang, L., 2017. Highly fractionated granites: Recognition and research. Sci. China Earth Sci. 60, 1201–1219.

Xia, X., Sun, M., Zhao, G., Wu, F., Xu, P., Zhang, J., Luo, Y., 2006. U–Pb and Hf isotopic study of detrital zircons from the Wulashan khondalites: Constraints on the evolution of the Ordos Terrane, Western Block of the North China Craton. Earth Planet. Sci. Lett. 241, 581–593.

Xia, Q.-K., Liu, J., Liu, S.-C., Kovács, I., Feng, M., Dang, L., 2013. High water content in Mesozoic primitive basalts of the North China Craton and implications on the destruction of cratonic mantle lithosphere. Earth Planet. Sci. Lett. 361, 85–97.

Xia, X.-P., Cui, Z.-X., Li, W., Zhang, W.-F., Yang, Q., Hui, H., Lai, C.-K., 2019. Zircon water content: reference material development and simultaneous measurement of oxygen isotopes by SIMS. J. Anal. At. Spectrom. 34, 1088–1097.

Yan, L.-L., He, Z.-Y., Beier, C., Klemd, R., 2018. Zircon trace element constrains on the link between volcanism and plutonism in SE China. Lithos 320-321, 28–34.

Zhang, W., Xia, X., Zhang, Y., Peng, T., Yang, Q., 2018. A novel sample preparation method for ultra-high vacuum (UHV) secondary ion mass spectrometry (SIMS) analysis. J. Anal. At. Spectrom. 33, 1559–1563.

Zhang, L., Ren, Z.Y., Xia, X.P., Yang, Q., Hong, L.B., Wu, D., 2019. In situ determination of trace elements in melt inclusions using laser ablation inductively coupled plasma sector field mass spectrometry. Rapid Commun. Mass Spectrom. 33, 361–370.